



HAL
open science

Direct Radiative Effect by Mineral Dust Aerosols Constrained by New Microphysical and Spectral Optical Data

Claudia Di Biagio, Yves Balkanski, Samuel Albani, O. Boucher, P. Formenti

► **To cite this version:**

Claudia Di Biagio, Yves Balkanski, Samuel Albani, O. Boucher, P. Formenti. Direct Radiative Effect by Mineral Dust Aerosols Constrained by New Microphysical and Spectral Optical Data. *Geophysical Research Letters*, 2020, 47 (2), 10.1029/2019GL086186 . hal-02505450

HAL Id: hal-02505450

<https://hal.science/hal-02505450>

Submitted on 3 Apr 2020

HAL is a multi-disciplinary open access archive for the deposit and dissemination of scientific research documents, whether they are published or not. The documents may come from teaching and research institutions in France or abroad, or from public or private research centers.

L'archive ouverte pluridisciplinaire **HAL**, est destinée au dépôt et à la diffusion de documents scientifiques de niveau recherche, publiés ou non, émanant des établissements d'enseignement et de recherche français ou étrangers, des laboratoires publics ou privés.

1 **Direct radiative effect by mineral dust aerosols constrained by new**
2 **microphysical and spectral optical data**

3 C. Di Biagio¹, Y. Balkanski², S. Albani^{2,3}, O. Boucher⁴, and P. Formenti¹

4 ¹ LISA, UMR CNRS 7583, Université Paris–Est–Créteil, Université de Paris, Institut Pierre–
5 Simon Laplace (IPSL), Créteil, France

6 ² Laboratoire des Sciences du Climat et de l’Environnement, CEA CNRS UVSQ UP Saclay,
7 Gif–sur–Yvette, France

8 ³ Department of Environmental and Earth Sciences, University of Milano–Bicocca, Milano, Italy

9 ⁴ Institut Pierre–Simon Laplace, CNRS / Sorbonne Université, Paris, France

10
11 Corresponding author: Claudia Di Biagio (claudia.dibiagio@lisa.u-pec.fr)

12
13 **Key Points:**

- 14 • New global dust simulations including particles >20 μm, refractive index representative of
15 world sources, and longwave scattering correction
16 • The global dust longwave effect remains within published values while the shortwave one
17 is reduced due to the inclusion of coarse particles
18 • Varying the longwave refractive index within its documented range of variability modifies
19 the sign of the net global dust direct effect

20

21 **Abstract**

22 We revise the direct radiative effect (DRE) of mineral dust aerosols in the shortwave (SW) and
23 longwave (LW) based on global model simulations that include coarse dust particles ($> 20 \mu\text{m}$)
24 and a new LW complex refractive index (CRI) dataset representative of major global sources.
25 Simulations are constrained against observed dust size distributions and optical depth. Scattering
26 of LW radiation is accounted for in the analysis. The extension of the dust size beyond $20 \mu\text{m}$
27 causes a reduction in the SW DRE compared to current model estimates, while the LW DRE
28 remains within published values due to compensating effects between changing size distribution,
29 CRI and accounting for dust scattering. The dust direct radiative effect efficiency from model
30 simulations reproduces well field observations close to sources and after transport. The global
31 mean net effect of dust is -0.03 Wm^{-2} as a result of cooling over oceans and warming over land.

32 **1. Introduction**

33 Whether desert dust aerosols warm or cool the planet by their direct radiative effect is still a
34 matter of debate (Boucher et al., 2013; Kok et al., 2017, hereafter Kok17). Dust particles of
35 diameter (D) smaller than $2 \mu\text{m}$ mostly cool our planet because scattering of SW radiation
36 dominates spectral absorption, while larger particles tend to cause warming by absorption of both
37 SW and LW radiation (Liao and Seinfeld, 1998; Miller et al., 2004. Mahowald et al., 2014).

38 Currently, global and regional models suffer from important deficiencies that introduce biases
39 in the estimated total dust DRE. These are:

- 40 1. Dust size distribution is often limited to a maximum diameter of typically 10 or $20 \mu\text{m}$ in
41 both regional and global models (Huneus et al., 2011; Kok17), neglecting the coarsest
42 particles which could contribute to positive DRE for both SW and LW radiation.
43 Furthermore recent field observations suggest that particles larger than $20 \mu\text{m}$ are present in
44 significant mass concentrations in the atmosphere (Ryder et al., 2013a, 2018, 2019; Weinzerl
45 et al., 2017; van der Does et al., 2018).
- 46 2. Modelled dust mass concentrations are usually under-estimated in models for particles with
47 $D > 5 \mu\text{m}$ and over-estimated for $D < 2 \mu\text{m}$ compared to observations (Kok, 2011; Kok17;
48 Ryder et al., 2019). Kok17 uses constraints on the size-dependency of the dust emissions to
49 fit field observations, which results in an average contribution of 4.3% for diameters smaller
50 than $2 \mu\text{m}$, significantly lower than the $5\text{--}35\%$ range in other models.
- 51 3. The variability in the dust complex refractive index at both SW and LW wavelengths, caused
52 by regional differences in the particle mineralogy (Sokolik and Toon, 1999), is not accounted
53 for in models. Global models commonly use the CRI of dust aerosols collected at Barbados
54 after being transported from the Sahara by Volz (1973) (hereafter V73) at LW wavelengths,
55 whereas different CRI datasets (Patterson et al., 1977; Shettle and Fenn, 1979; d'Almeida et
56 al., 1991) are used in the SW. Recent laboratory measurements of dust samples collected
57 over many different deserts suggest that the imaginary part of the SW and LW CRI as
58 assumed in models are upper bound values that can lead to a strong overestimate of the dust

59 spectral absorption and biases in DRE (Di Biagio et al., 2017, hereafter DB17; Di Biagio et
60 al., 2019).

- 61 4. Most global and regional models do not include LW scattering in their radiative scheme.
62 However, the contribution of scattering is relevant as it could increase the LW DRE at the
63 Top-of-the-Atmosphere (TOA) by 50% (Dufresne et al., 2002; Sicard et al., 2014; Osipov
64 et al., 2015). Up to now only two studies (Miller et al., 2006; Kok17) try to account for
65 missing LW scattering by artificially augmenting the retrieved TOA DRE by 23%.
66 Nonetheless, this correction represents only about half of the value inferred by Dufresne et
67 al. (2002), Sicard et al. (2014), and Osipov et al. (2015).
- 68 5. Dust particles are usually assumed as spherical in models. While this simplification may
69 considerably impact the extinction efficiency (Q_{ext}) and AOD calculations (Dubovik et al.,
70 2006; Kok17, Potenza et al., 2016), it was demonstrated to have only a limited influence on
71 the TOA DRE (considering a more realistic phase function results in less than 5% and 10%
72 difference compared to spherical dust in the SW and LW ranges, Bellouin et al., 2004;
73 Colarco et al., 2014; however, a larger effect might be expected if a Bidirectional Reflectance
74 Distribution Function, BRDF, surface albedo is assumed in models, Osipov et al., 2015).

75 In this study we present a novel evaluation of the global DRE by mineral dust aerosols and
76 its SW and LW components based on new global model simulations. We constrain the size
77 distribution of dust in the source regions and its AOD at 550 nm (AOD_{550}) in our simulations based
78 on field observations, incorporating dust sizes beyond 20 μm diameter. We correct the dust DRE
79 for accounting the LW scattering effect following Dufresne et al. (2002). For the first time in global
80 simulations we take into account regional variations of the LW CRI, as documented in DB17, to
81 estimate the dust spectral optical properties. In the present study we assume that dust particles are
82 spherical.

83 We compare simulated dust SW and LW direct radiative effect efficiency (DREE) with
84 available observations (including space-borne sensors) over Northern Africa, Asia, the Atlantic
85 Ocean, and the Mediterranean basin.

86 **2. Method**

87 Global aerosol simulations are performed with the LMDZOR-INCA model (Schulz, 2007;
88 Balkanski et al., 2010) which couples interactively the LMDZ (Laboratoire de Météorologie
89 Dynamique) atmospheric General Circulation Model, the ORCHIDEE land surface model and the
90 INCA (INteraction with Chemistry and Aerosols) aerosol module. The radiative transfer module
91 includes a six-band (0.185–4.0 μm) version of the Fouquart and Bonnel (1980) scheme in the SW
92 and the RRTMG (Rapid Radiative Transfer Model for Global Circulation Models) radiative
93 scheme in sixteen bands between 3.33 and 1000 μm .

94 **2.1 Constraining the size distribution of dust aerosols**

95 A superposition of lognormal modes is used to represent the aerosol size distribution in
96 LMDZOR-INCA (Schulz, 2007). Each mode is described by two variables: a Mass Median

97 Diameter (MMD) and a geometric standard deviation (σ). The MMD in each mode varies during
98 the simulation in order to account for all processes that increase or deplete the aerosol atmospheric
99 concentration. In contrast, the width of the size distribution (measured by σ) is kept constant. The
100 shape of the dust size distribution at emission is constrained by fitting the dataset recently used by
101 Kok17 (**Fig. 1a**), but augmented to include missing particles larger than 20 μm with airborne
102 measurements taken during the FENNEC campaign in Western Sahara for airborne dust less than
103 12 hours after emission (Ryder et al., 2013a, 2013b) (**Fig. 1b**). FENNEC is the only campaign that
104 measured the dust size distribution up to 150 μm in diameter very close to source areas. We fit the
105 extended size distribution with four lognormal modes with respective MMD equal to 1 μm ($\sigma=1.8$),
106 2.5 μm ($\sigma=2$), 7 μm ($\sigma=1.9$), and 22 μm ($\sigma=2$). The relative mass contribution (m_i) by each mode
107 to the total emitted size, retrieved by fitting the ensemble of the observational dataset, is 0.6%
108 ($\pm 0.1\%$), 4.3% ($\pm 0.4\%$), 31.5% ($\pm 1.8\%$) and 63.6% ($\pm 2.2\%$) for modes at 1, 2.5, 7, and 22 μm
109 MMD, respectively (Fig. 1b). The ratio of the PM_2 ($D \leq 2 \mu\text{m}$) to PM_{20} ($D \leq 20 \mu\text{m}$) emitted mass
110 is 4.7%, within the 3.5–5.7% range indicated by Kok17.

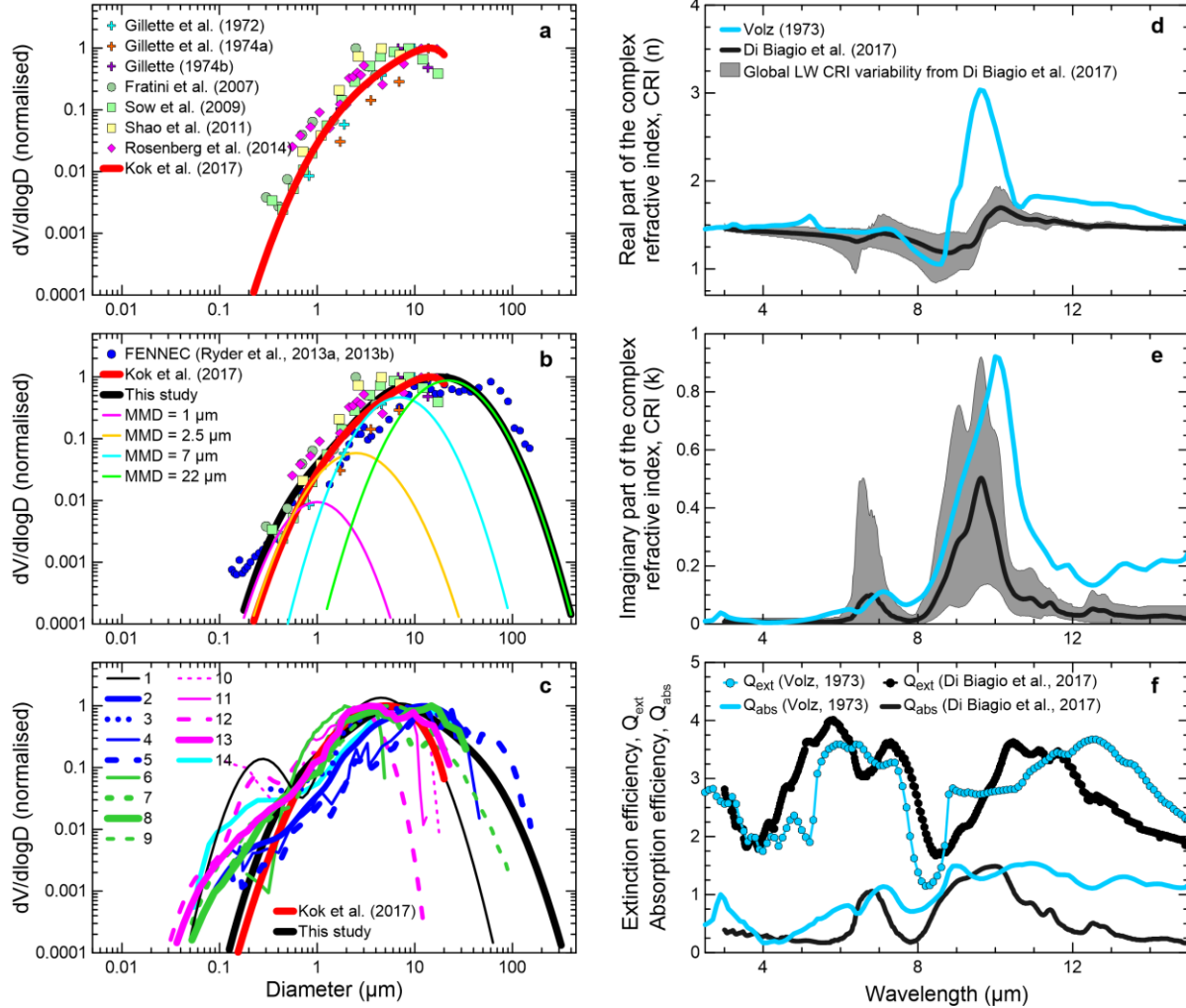
111 The average size distribution of atmospheric dust is in agreement with in situ and remote
112 sensing field observations taken after few days of transport in Northern Africa, the Mediterranean,
113 and across the Atlantic Ocean (Fig. 1c). The model captures well the coarse component of the dust
114 size as measured in the field but does not represent the peaks in volume distribution below about
115 0.5 μm shown in field data, which are documented to consist of fine anthropogenic particles mixed
116 in the dust plume (Chou et al., 2008; Kandler et al., 2011).

117 The size-resolved dust load in our model also agrees with new field observations indicating
118 that, after few days of transport at Cape Verde, dust particles larger than 5 μm (20 μm) account for
119 60% (0–12%) of the mass (Ryder et al., 2019). Our model data extracted over the same area and
120 time period show 63% and 11.5% of the mass for $D > 5 \mu\text{m}$ and $D > 20 \mu\text{m}$, respectively.

121 **2.2 Constraining the spectral CRI of dust**

122 To further constrain simulations we use a novel observational dataset of regionally-averaged
123 LW CRI published by DB17 for nineteen natural dust aerosol samples collected in arid and semi-
124 arid regions of the world (Africa, Asia, America, Australia). These nineteen samples were selected
125 from a much larger assemblage to represent the global variability of the dust content of LW-active
126 minerals (clays, quartz, and calcite), and therefore of LW CRI. Published radiative closure studies
127 based on aircraft radiation data (Meloni et al., 2018; Granados-Muñoz et al., 2019) and satellite
128 radiance observations (Liuzzi et al., 2017; Banks et al., 2018; Song et al., 2018) confirm the
129 improved capability of the DB17 dataset to represent the regional variations in the dust LW DRE
130 compared to the V73 CRI.

131



132

133 ¹ Dubovik et al. (2002); ² Weinzierl et al. (2009); ³ Formenti et al. (2011); ⁴ Ryder et al. (2013b) – SAL (Saharan Air Layer); ⁵ Ryder et al.
 134 (2013b) – aged dust; ⁶ Chen et al. (2011); ⁷ Weinzierl et al. (2011); ⁸ Weinzierl et al. (2017) – Cape Verde; ⁹ Ryder et al. (2018); ¹⁰
 135 Formenti et al. (2001); ¹¹ Maring et al. (2003); ¹² Denjean et al. (2016b); ¹³ Weinzierl et al. (2017) – Barbados. ¹⁴ Denjean et al. (2016a)

136 **Figure 1.** Volume size distributions $dV/d\log D$ and longwave optical properties of the dust aerosols. **a** Size
 137 distribution of the emitted dust reported by Kok17 (Kok et al., 2017) obtained by fitting the reported dataset
 138 ensemble. **b** Size distribution of the emitted dust retrieved in this study. Similar to panel a, the distribution is
 139 obtained by fitting the Kok17 dataset ensemble but also includes the FENNEC dataset that represents fresh
 140 dust (<12 h from emission). The contribution by the four different modes to our fitted size is shown. **c.**
 141 Globally-averaged atmospheric dust size distribution obtained from model simulations in this study (weighted
 142 by the global mass load of each mode) and in Kok17. Field data from campaigns in Northern Africa (blue
 143 lines), the Mediterranean (cyan lines), eastern Atlantic Ocean (green lines) and Western Atlantic Ocean (pink
 144 lines) are shown for comparison. Retrieved dust size from AERONET is also reported. All size data in panels
 145 a–c, including the scattering data and the fitting lines from Kok17, are normalized to 1 at the maximum of the
 146 volume distribution. **d–e** Longwave real and imaginary parts of the CRI from V73 (Volz, 1973) and DB17 (Di
 147 Biagio et al., 2017). The black line represents the average spectral values from DB17, while the shaded grey
 148 area envelopes the minimum and the maximum of the DB17 dataset representing the CRI regional variability.
 149 **f** Spectral absorption (Q_{abs}) and extinction (Q_{ext}) efficiencies estimated from Mie calculations for a particle of
 150 $D = 10 \mu\text{m}$ and V73 and DB17 CRI.

151 In the present study, the base model simulations use the mean wavelength–dependent LW
152 CRI values by DB17. The minimum and maximum of the imaginary part from DB17 (and
153 associated real parts from Kramers–Kronig relationships) serve to represent the envelope of the
154 regional variations in CRI. **Figure 1d–f** illustrates the important finding that the imaginary parts
155 of the CRI from DB17 is lower than reported by V73, resulting in a lower absorption over most of
156 the spectrum. **Figure 1f** also illustrates the relative importance of scattering versus absorption at
157 longwave wavelengths, i.e. Q_{abs} is only a fraction of Q_{ext} .

158 In the SW range we employ the spectral CRI from Balkanski et al. (2007) computed assuming
159 that dust contains an average 1.5% of hematite by volume. This assumption corresponds to 1.52–
160 0.0017i at 550 nm and proved to produce good agreement of the simulated SW TOA DRE and
161 satellite observations (Balkanski et al., 2007). This SW CRI falls at the mean of the values recently
162 reported by Di Biagio et al. (2019) for dust from major global sources.

163 **2.3 Constraining the dust emission flux, atmospheric load and optical depth**

164 The total emission flux (E_{tot}) is 13689 Tg yr⁻¹ in our simulations, amounting to 5023 Tg yr⁻¹
165 for $D > 20 \mu\text{m}$ and 8666 Tg yr⁻¹ for $D \leq 20 \mu\text{m}$, a value that is at the upper bound of the emission
166 flux range obtained by Escrivano et al. (2017) through a source inversion approach. The E_{tot} is
167 partitioned between the four modes following their mass percent contribution to the emitted size,
168 resulting in $E_1=80$, $E_{2.5}=584$, $E_7=4308$, and $E_{22}=8717$ Tg yr⁻¹, respectively. We set the E_{tot} value
169 in order to have a resulting global and annual mean dust AOD₅₅₀ within the range from recent
170 synthesis of observations (0.030 ± 0.005) (Ridley et al., 2016) and at the same time both the PM₁₀
171 ($D \leq 10 \mu\text{m}$) and PM₂₀ dust loads the closest as possible to the reported range by Kok17 (13–29
172 Tg and 14–33 Tg, respectively). The dust AOD₅₅₀ in our simulations is 0.026 for a total load of
173 38.9 Tg, of which 26 Tg for PM₁₀ and 34.1 Tg for PM₂₀.

174 **2.4 Global simulations and DRE estimate**

175 We run the model separately for each of the four size modes and for the multimodal size
176 distribution. Emission is set at E_1 , $E_{2.5}$, E_7 , and E_{22} for single–mode simulations and at E_{tot} for the
177 combined multimodal run. We repeat single–mode simulations by assuming different LW CRI
178 datasets (mean, min, max from DB17 and V73). For the multimodal simulation we assume the
179 mean LW CRI from DB17 only. A reference simulation with no dust aerosols is performed.

180 The SW and LW DRE at the TOA and at the surface are calculated for clear– and all–sky
181 conditions as the difference in shortwave and longwave radiative fluxes with and without dust.
182 The dust feedbacks on climate are not activated in our simulations, i.e. dust is a passive tracer, and
183 the perturbation to radiative fluxes from dust is only diagnostic.

184 The dust AOD₅₅₀ and the DRE are averaged spatially (globally or over specific regions) and
185 temporally (annually or monthly/seasonally) for the evaluation of the global and annual averages
186 and for comparison with satellite and field observations. The SW and LW DREE is calculated as
187 the ratio of the DRE to AOD₅₅₀.

188 As longwave scattering by dust is not accounted for in the model radiative scheme, we
189 correct the LW DRE assuming a multiplicative factor of 2.04 (± 0.18) (unitless) at TOA and 1.18
190 (± 0.01) at the surface based on Dufresne et al. (2002). This corresponds to 51% contribution of
191 scattering to the LW DRE at TOA and 15% at the surface. Note that this correction, estimated for
192 dust of $D \leq 10 \mu\text{m}$, might be a lower approximation of the LW scattering by coarse dust.

193 The uncertainty on the dust DRE and DREE arises from a combination of uncertainties in
194 the: (i) emissions, representation of the size distribution of dust and its spatio-temporal variability
195 (i.e., transport and deposition processes in model), which can be expressed as a single uncertainty
196 of the model skill to simulate the dust AOD_{550} ; (ii) dust vertical profile; (iii) refractive index
197 assumptions and its global variability; (iv) dust shape assumptions; (v) treatment of aerosol-
198 radiation interactions; and (vi) host model uncertainties. The overall uncertainty on the dust DRE
199 is calculated by adding in quadrature all listed uncertainties in the assumption that error sources
200 are independent. The resulting relative uncertainty on the global annual mean TOA DRE (DREE)
201 is estimated to be 85% (88%) in the SW and 69% (72%) in the LW as 90% confidence intervals
202 (CI). More details are provided in the Supplementary Information.

203 3. Results

204 3.1 Model-observations comparison of the dust radiative effect efficiency

205 **Table 1** shows the comparison of our model estimates of the clear-sky SW and LW DREE
206 with those reported by field studies based on satellite and ground-based observations. Comparing
207 the DREE allows eliminating differences due to the variable regional load, optically represented
208 by the AOD_{550} . Observations correspond to monthly and seasonal averages in different regions
209 close to African and Asian sources and along the transport pathway straddling along the Atlantic
210 Ocean and the Mediterranean.

211 The DREE values from model simulations are in good agreement with observations in the LW.
212 Using the CRI by DB17 allows reproducing observations within the uncertainty range, both close
213 to the sources and remotely. Results for the V73 CRI are most of the time at the upper bound of
214 field retrieved DREE intervals. Several field studies considered for comparison make use of a
215 certain degree of modelling to derive the dust DREE. Our model results for DREE LW are in best
216 agreement with those providing observational-only estimates.

217 The DREE comparison is generally worse in the SW, but a very good agreement is obtained
218 over the Tropical Atlantic. Differences in the SW range may arise from the different spectral
219 coverage between the observational products and the model, and also the different methods applied
220 for DREE retrieval and averaging (see Supplementary Information).

221 Note that the total DREE computed by adding up the DRE from single mode simulations is up
222 to 30% (SW) and 7% (LW) lower in absolute value than obtained from the multimodal run.

223

224

| Shortwave spectral range | | | | | | | |
|--------------------------------------|-------------------|-------------------------------------|---------|--------------------------------|--------------------------------|-----------------------|----------------------|
| Geographical zone | Temporal interval | Platform | Level | DREE field (Wm ⁻²) | DREE model (Wm ⁻²) | | |
| | | | | | CRI= B07 SIZE= SM | CRI= B07 SIZE= MM | |
| Sahara desert (15°–30°N, 10°W– 30°E) | JJA | Satellite and model ^a | TOA | ~0 | 11.6 | 10.5 | |
| Tropical Atlantic (15–25N, 15–45W) | JJA | Satellite ^b | TOA | –35 | –31.6 | –28.0 | |
| | | | surface | –65 | –62.6 | –58.3 | |
| Tropical Atlantic (10–30N, 20–45W) | JJA | Satellite ^c | TOA | –28 | –35.9 | –32.7 | |
| Atlantic Ocean (0–30N, 10–60W) | JJA | Satellite ^d | TOA | –42 to 54 | –23.7 | –21.6 | |
| Mediterranean basin (35.5N, 12.6E) | Sept | Ground–based ^{e–f} | surface | –68.8 | –68.0 | –65.8 | |
| | | | TOA | –45.5 | –35.5 | –33.6 | |
| China (39N, 101E) | AMJ | Ground–based ^g | surface | –60 | –44.6 | –34.3 | |
| Longwave spectral range | | | | | | | |
| Geographical zone | Temporal interval | Platform | Level | DREE field (Wm ⁻²) | DREE model (Wm ⁻²) | | |
| | | | | | CRI= DB17 SIZE= SM | CRI= DB17 SIZE= MM | CRI= V73 SIZE= SM |
| North Africa (15–35N, 18W–40E) | JJA | Satellite ^{h–i} | TOA | 15–22 | 14.9 | 14.1 | 27.1 |
| West Africa (16–28N, 16–4W) | JJA | Satellite ^{h–i} | TOA | 16–20 | 15.2 | 14.3 | 26.9 |
| Niger–Chad (15–20N, 15–22E) | JJA | Satellite ^{h–i} | TOA | 16–21 | 16.5 | 15.9 | 30.0 |
| Sudan (15–22N, 22–36E) | JJA | Satellite ^{h–i} | TOA | 19–23 | 14.4 | 14.1 | 27.4 |
| Egypt–Israel (23–32N, 23–35E) | JJA | Satellite ^{h–i} | TOA | 1–27 | 14.0 | 14.0 | 27.4 |
| North Libya (27–33N, 15–25E) | JJA | Satellite ^{h–i} | TOA | 11–25 | 13.4 | 12.9 | 24.6 |
| South Libya (23–27N, 15–25 E) | JJA | Satellite ^{h–i} | TOA | 11–22 | 14.3 | 14.0 | 26.9 |
| Sahara desert (15–30N, 10W– 30E) | JJA | Satellite ^j | TOA | 11–26 | 15.9 | 15.1 | 27.9 |
| Tropical Atlantic (10–30N, 20–45W) | JJA | Satellite ^c | TOA | 8.5 | 8.8 | 8.7 | 16.8 |
| Atlantic Ocean (0–30N, 10–60W) | JJA | Satellite ^d | TOA | 2.6–11.4 | 10.7 | 10.3 | 19.9 |
| Cape Verde (16.7N, 22.9W) | Sept | Ground–based and model ^k | TOA | 13 | 9.3 | 8.9 | 17.2 |
| | | | surface | 16 | 15.6 | 14.6 | 25.4 |
| China (39N, 101E) | AMJ | Ground–based ^g | TOA | 17–21 | 9.3 | 7.7 | 16.1 |
| | | | surface | 31–35 | 20.5 | 16.0 | 34.9 |

225 ^a Patadia et al. (2009); ^b Li et al. (2004); ^c Song et al. (2018); ^d Christopher and Jones (2007); ^e di Sarra et al. (2008); ^f Di Biagio et al. (2010);
226 ^g Hansell et al. (2012); ^h Zhang and Christopher (2003); ⁱ Brindley and Russel (2009); ^j Yang et al. (2009); ^k Hansell et al. (2010)

227 JJA = June–July–August, AMJ = April–Mai–June; SM = Single modes simulations (sum of single modes DRE); MM = Multimodal size
228 distribution simulations; B07 = Balkanski et al. (2007); DB17 = Di Biagio et al. (2017); V73= Volz (1973)

229

230 **Table 1.** Model–observations comparison of the shortwave and longwave dust clear–sky direct radiative effect
231 efficiency (DREE) at the surface and the Top–of–the–Atmosphere (TOA) for different size assumptions and
232 complex refractive index (CRI) data. We indicate in blue the studies that do not rely on modelling to derive the
233 DREE.

3.2 Dust global DRE: role of coarse particles and sensitivity to the refractive index

Table 2 summarizes the contribution of dust particles of different sizes and CRI to the various processes and variables in our simulations. The global annual mean all-sky DRE of mineral dust at TOA is -0.25 W m^{-2} (-0.04 to -0.46 W m^{-2} , 90% CI) for the SW and $+0.22 \text{ W m}^{-2}$ ($+0.07$ to $+0.37 \text{ W m}^{-2}$, 90% CI) for the LW as obtained for the multimodal simulation. The net TOA DRE is -0.03 W m^{-2} , which corresponds to -0.29 to $+0.23 \text{ W m}^{-2}$ within 90% CI. The value of the net TOA DRE is given by the sum of a positive effect over land and a negative effect over oceans, particularly over the Northern Hemisphere where most of the dust is found.

The modes at 1 and 2.5 μm account for a tiny fraction of emission (less than 5%) but are responsible for 21% of the dust load, 57% of AOD_{550} and most of the SW cooling. The opposite is true for the mode at 22 μm that represents 64% of emission but only 17% of load, 3% of AOD_{550} and has a lower but not negligible contribution to both SW and LW DRE. In contrast, the mode at 7 μm amounts to 32% of emission, 60% of load, 40% of AOD_{550} and more than 60% of DRE LW. The fraction of dust above 20 μm diameter is estimated from modes at 7 and 22 μm to contribute to 37% of the total emission, 12% of the load, and 2% of the AOD_{550} , and to account for about 30% of the DRE of the mode at 22 μm . The key role of particles larger than 20 μm however does not only rely on their direct contribution to the DRE, but mostly on the fact that their inclusion reduces the contribution by smaller (cooling) particles to the global dust cycle.

The SW DRE is negative (cooling) for the 1, 2.5, and 7 μm modes and positive (warming) for the 22 μm mode, while the total (SW+LW) effect is negative for the 1 and 2.5 μm modes and positive for the 7 and 22 μm modes. These global values mask the sharp contrast existing between the positive SW values in the vicinity of source regions and the negative values over oceanic areas, as can be seen in Table 2 comparing TOA DRE over the Sahara desert and the Tropical Atlantic.

Using the V73 CRI data results in a LW DRE of $+0.42 \text{ W m}^{-2}$, with a net SW+LW positive effect of $+0.13 \text{ W m}^{-2}$ (sum of single mode simulations). Using the mean CRI data from DB17 reduces the LW DRE by almost a factor two for each mode simulation compared to V73. Varying the LW CRI between the minimum and maximum of the values indicated by DB17 also changes the sign of the net DRE from -0.19 to $+0.08 \text{ W m}^{-2}$ due to the variation of the DRE LW between $+0.09 \text{ W m}^{-2}$ and $+0.36 \text{ W m}^{-2}$, respectively. The CRI is therefore one of the largest source of uncertainty of the dust DRE.

| | Mode 1 MMD=1 μ m NMD=0.35 μ m σ =1.8 | Mode 2 MMD=2.5 μ m NMD=0.59 μ m σ =2 | Mode 3 MMD=7 μ m NMD=2.03 μ m σ =1.9 | Mode 4 MMD=22 μ m NMD=5.21 μ m σ =2.0 | Total | |
|---|---|---|---|--|-------------------------|-------------------|
| % mass fraction (m_i) ($\pm 1\sigma$) for dust size at emission from fitting field observations | 0.6 (± 0.1) | 4.3 (± 0.4) | 31.5 (± 1.8) | 63.6 (± 2.2) | | |
| Emission rate (Tg yr⁻¹) | 80 | 584 | 4308 | 8717 | 13689 | |
| Emission PM ₂ (Tg yr ⁻¹) | 70 | 220 | 112 | 2 | 405 | |
| Emission PM ₂₀ (Tg yr ⁻¹) | 80 | 584 | 4092 | 3910 | 8666 | |
| Emission D>20 μ m (Tg yr ⁻¹) | 0 | 0 | 216 | 4807 | 5023 | |
| Load (Tg) | 1.2 | 7.0 | 24.2 | 6.5 | 38.9 | |
| Load PM ₂ (Tg) | 1.0 | 2.7 | 0.6 | 0 | 4.3 | |
| Load PM ₂₀ (Tg) | 1.2 | 7.0 | 23.0 | 2.9 | 34.1 | |
| Load D>20 μ m (Tg) | 0 | 0 | 1.2 | 3.6 | 4.8 | |
| Lifetime (days) | 5.4 | 4.4 | 2.0 | 0.3 | 1.0 | |
| AOD₅₅₀ | 0.0045 | 0.0105 | 0.0106 | 0.0009 | 0.0265 | |
| AOD ₅₅₀ PM ₂ | 0.0044 | 0.0073 | 0.0019 | 0 | 0.014 | |
| AOD ₅₅₀ PM ₂₀ | 0.0045 | 0.0104 | 0.0105 | 0.0006 | 0.026 | |
| AOD ₅₅₀ D>20 μ m | 0 | 0.0001 | 0.0001 | 0.0003 | 0.0005 | |
| | Mode 1 MMD=1 μ m NMD=0.35 μ m σ =1.8 | Mode 2 MMD=2.5 μ m NMD=0.59 μ m σ =2 | Mode 3 MMD=7 μ m NMD=2.03 μ m σ =1.9 | Mode 4 MMD=22 μ m NMD=5.21 μ m σ =2.0 | Sum single modes | Multimodal |
| Direct Radiative Effect at TOA (Wm⁻²), global annual mean all-sky, mean LW CRI from DB17 | | | | | | |
| SW | -0.09 | -0.18 | -0.03 | +0.02 | -0.29 | -0.25 |
| LW | +0.01 | +0.06 | +0.14 | +0.02 | +0.23 | +0.22 |
| NET (SW+LW) | -0.08 | -0.13 | +0.11 | +0.04 | -0.06 | -0.03 |
| Direct Radiative Effect at TOA (Wm⁻²), global annual mean all-sky, min LW CRI from DB17 | | | | | | |
| LW | +0.00 | +0.02 | +0.06 | +0.01 | +0.09 | - |
| NET (SW+LW) | -0.09 | -0.16 | +0.03 | +0.03 | -0.19 | - |
| Direct Radiative Effect at TOA (Wm⁻²), global annual mean all-sky, max LW CRI from DB17 | | | | | | |
| LW | +0.02 | +0.11 | +0.21 | +0.02 | +0.36 | - |
| NET (SW+LW) | -0.07 | -0.07 | +0.18 | +0.04 | +0.08 | - |
| Direct Radiative Effect at TOA (Wm⁻²), global annual mean all-sky, CRI from V73 | | | | | | |
| LW | +0.02 | +0.10 | +0.27 | +0.03 | +0.42 | - |
| NET (SW+LW) | -0.08 | -0.08 | +0.24 | +0.05 | +0.13 | - |
| Net (SW+LW) Direct Radiative Effect at TOA (Wm⁻²), annual mean all-sky, mean LW CRI from DB17 | | | | | | |
| Northern hemisphere land | -0.23 | -0.24 | 0.63 | 0.18 | 0.33 | 0.39 |
| Northern hemisphere ocean | -0.17 | -0.23 | -0.05 | 0.01 | -0.44 | -0.33 |
| Southern hemisphere land | -0.02 | -0.03 | 0.00 | 0.01 | -0.04 | -0.04 |
| Southern hemisphere ocean | -0.01 | -0.01 | 0.00 | 0.00 | -0.02 | -0.02 |
| Tropical Atlantic (15–25N,15–45W) | -1.05 | -2.12 | -0.37 | 0.14 | -3.40 | -2.78 |
| Sahara (18– 35N, 18 W–40 E) | -0.53 | 0.02 | 3.38 | 0.93 | 3.79 | 3.65 |
| Sahel (11–18N, 18 W – 22.5 E) | -1.26 | -1.22 | 3.50 | 0.93 | 1.95 | 2.34 |
| Middle East (15–40N, 40–60 E) | -0.38 | -0.53 | 0.68 | 0.17 | -0.05 | 0.07 |
| Eastern Asia (30–50 N, 75–130 E) | -0.52 | -0.90 | 0.32 | 0.23 | -0.87 | -0.44 |

270

271 **Table 2.** Summary of results of our global simulations. We report the contribution of dust particles of different
272 sizes and complex refractive index (CRI) to emissions, atmospheric load, lifetime, AOD₅₅₀, and the shortwave
273 (SW), longwave (LW), and net direct radiative effect (DRE).

274

275

4. Discussion: towards an observationally–constrained dust DRE

276

277

278

279

280

281

Figure 2 summarizes recent developments resulting from applying observational constraints to dust global models including size and optical properties. The inclusion of the coarse mode up to 20 μm in Kok17 and its further extension in the present study leads to a progressive reduction of the SW cooling when compared to the AEROCOM (Aerosol Comparisons between Observations and Models, Huneeus et al., 2011) estimate for PM_{10} dust (-0.65 Wm^{-2} median value in AEROCOM models, -0.49 Wm^{-2} in Kok17, -0.25 Wm^{-2} in the present study).

282

283

284

285

286

287

We assume for the first time a LW CRI constrained by laboratory measurements, and we also account for the strong scattering effect of dust in the same spectral range. Our estimated dust LW DRE of $+0.22 \text{ Wm}^{-2}$ is in between the AEROCOM median estimate of $+0.15 \text{ Wm}^{-2}$ and the $+0.29 \text{ Wm}^{-2}$ published by Kok17. The LW DRE represents on average between 23 and 59% of the SW perturbation at TOA from past literature. Here, the LW contribution amounts to 88% of the SW term at TOA.

288

289

290

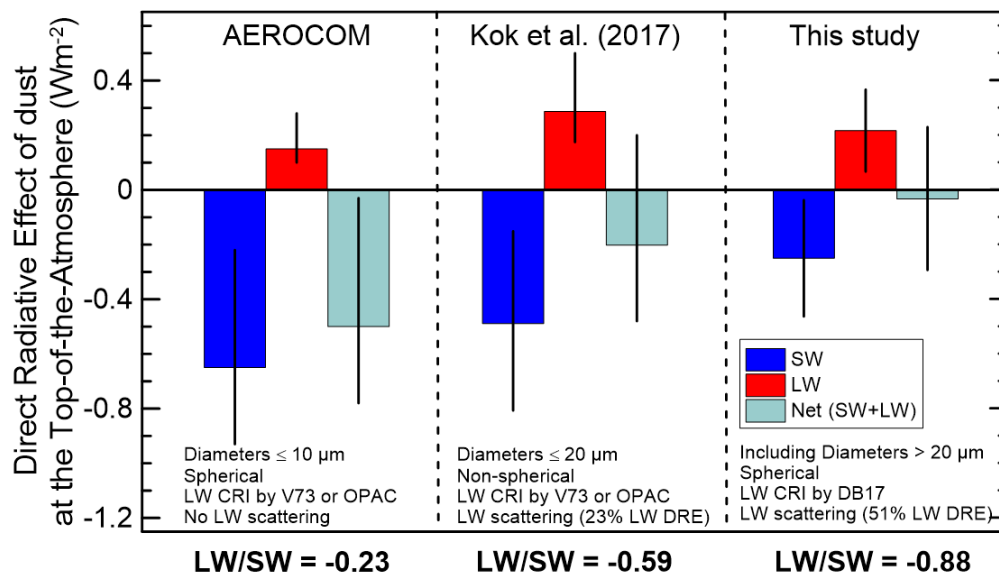
291

292

293

The reduction of SW cooling and the increase of the LW/SW ratio also result in a progressive reduction of the net DRE from the strong negative values of AEROCOM (-0.50 Wm^{-2}) to our estimate of -0.03 Wm^{-2} . However, we stress that because net TOA DRE is geographically varying and can have opposing sign, this can hide large impacts with potentially relevant implications for regional climate (Albani and Mahowald, 2019). In analogy with their study, we report an absolute value of net TOA DRE (global annual average) of 0.32 Wm^{-2} .

294



295

296

297

298

299

300

301

Figure 2. Top-of-the-atmosphere global annual mean all-sky shortwave (SW), longwave (LW), and net dust direct radiative effect as obtained in AEROCOM models, in Kok et al. (2017) and in this study. AEROCOM estimate is from Figure 4 in Kok et al. (2017). The inserts detail main assumptions including the used complex refractive index (CRI) data (OPAC is Optical properties of Aerosols and Clouds, Hess et al., 1998), if the LW scattering correction is applied and its percentage of the TOA LW DRE.

5. Conclusions

Our model simulations indicate that the global net DRE of dust is close to zero, due to almost opposing SW (cooling) and LW (warming) effects. This global value is also the result of the sum of a positive effect over land, in particular over the Sahara, and a negative effect over oceans.

We find that accounting for dust beyond 20 μm diameter reduces the SW cooling compared to previous studies, while the LW DRE remains in the range of previous estimates due to the compensating effects of updating size, LW CRI and scattering. Based on our sensitivity calculations we stress the importance of including regional differences in the CRI and a more realistic representation of the dust size distribution and LW scattering both in global and regional models since they affect the magnitude and sign of the dust DRE. Also, we highlight the necessity for more field measurements to better constrain the emitted dust size distribution at $D \geq 20 \mu\text{m}$.

Our results suggest that current climate models might significantly overestimate the dust global cooling effect, thus also biasing estimates of the total aerosol radiative perturbation. Although it remains an open question whether global dust loading will increase or decrease in the future, our study indicates that the spatial variability of dust net DRE could be more complex than previously thought in driving global feedbacks, with a potentially important role of dust DRE on regional climate.

Acknowledgements

The laboratory experiments to retrieve the dust refractive indices in Di Biagio et al. (2017) that feed this work had received funding from the European Union's Horizon 2020 research and innovation program through the EUROCHAMP-2020 Infrastructure Activity under grant agreement no. 730997. They were supported by the French national programme LEFE/INSU (Les Enveloppes Fluides et l'Environnement / Institut National des Sciences de l'Univers) and by the OSU-EFLUVE (Observatoire des Sciences de l'Univers-Enveloppes Fluides de la Ville à l'Exobiologie) through dedicated research funding to the RED-DUST project. The authors acknowledge the CNRS-INSU for supporting the CESAM chamber as national facility and the AERIS datacenter (www.aeris-data.fr) for distributing and curing the data produced by the CESAM chamber through the hosting of the EUROCHAMP datacenter (<https://data.eurochamp.org>). The present project conducted at IPSL (Institut Pierre Simon Laplace) used the HPC (High Performance Computing) resources of TGCC (Très Grand Centre de calcul du CEA, Commissariat à l'énergie atomique et aux énergies alternatives) under the allocations 2018-A0050102201, and 2019-A0050102201 (project gen2201) provided by GENCI (Grand Équipement National de Calcul Intensif). Y. Balkanski and O. Boucher were partly supported by the CRESCENDO project, funded by the European Union's Horizon 2020 programme, Grant Agreement no. 641816. C. Di Biagio was supported by the CNRS via the Labex L-IPSL, which is funded by the ANR (grant no. ANR-10-LABX-0018). S. Albani acknowledges

340 funding from the European Union’s Horizon 2020 research and innovation programme under the
341 Marie Skłodowska–Curie grant agreement No 708119, for the project “DUSC, Climate, and the
342 Carbon Cycle” (DUSC3). The authors wish to acknowledge C. Denjean, C. L. Ryder, and J. Kok
343 for providing the size distribution data shown in Fig. 1. C. Di Biagio also wishes to thank J. Kok
344 and J.–L. Dufresne for useful discussions. The authors wish to thank the reviewers, Y. Huang and
345 S. Osipov, for their helpful comments that helped to improve the quality of the paper.
346

347 **Data availability**

348 The LMDZOR–INCA input data, run configuration and output diagnostic variables are publicly
349 available at <http://doi:10.5281/zenodo.3531929>. Complex refractive indices from Di Biagio et al.
350 (2017) used here are freely available within the Library of Advanced Data Products (LADP) of the
351 EUROCHAMP datacenter (<https://data.eurochamp.org/data-access/optical-properties/>). The
352 complex refractive index data from Volz (1973) are available at <http://eodg.atm.ox.ac.uk/ARIA/>.
353 The size data used for comparison in Fig. 1c and the satellite data in Table 1 are described in the
354 Supplementary Information and accessible from the main publications. Data in Fig. 3 are available
355 from Kok et al. (2017) and the present study.
356

357 **Conflicts of interest**

358 The authors declare no conflicts of interests.
359

360 **References**

- 361 Albani, S., & Mahowald, N. (2019). Paleodust insights into dust impacts on climate. *Journal of*
362 *Climate*, **32**, 7897–7913, <https://doi.org/10.1175/JCLI-D-18-0742.1> .
- 363 Balkanski Y., D. Jacob, G. Gardner, W. Graustein, And K. K. Turekian (1993). Tropospheric
364 Residence Times of Continental Aerosols derived from a Three Dimensional Simulation of
365 210Pb, *Journal of Geophysical Research: Atmosphere*, **98**, pp. 20573–20586.
- 366 Balkanski, Y., Schulz, M., Claquin, T., Moulin, C., & Ginoux, P. (2004). Global Emissions of
367 Mineral Aerosol: Formulation and Validation using Satellite Imagery, Springer Netherlands,
368 Dordrecht, 239–267, https://doi.org/10.1007/978-1-4020-2167-1_6.
- 369 Balkanski, Y., Schulz, M., Claquin, T., & Guibert, S. (2007). Reevaluation of Mineral aerosol
370 radiative forcings suggests a better agreement with satellite and AERONET data. *Atmospheric*
371 *Chemistry and Physics*, **7**, 81–95, <https://doi.org/10.5194/acp-7-81-2007>.
- 372 Balkanski, Y., Myhre, G., Gauss, G., Rädcl, G., Highwood, E.J., & Shine, K. P. (2010). Direct
373 radiative effect of aerosols emitted by transport: from road, shipping and aviation. *Atmospheric*
374 *Chemistry and Physics* , **10**, 4477–4489, <https://doi.org/10.5194/acp-10-4477-2010>.
- 375 Banks, J. R., Schepanski, K., Heinold, B., Hünerbein, A., & Brindley, H. E. (2018). The influence
376 of dust optical properties on the colour of simulated MSG–SEVIRI Desert Dust infrared
377 imagery. *Atmospheric Chemistry and Physics*, **18**, 9681–9703, [https://doi.org/10.5194/acp-18-](https://doi.org/10.5194/acp-18-9681-2018)
378 [9681-2018](https://doi.org/10.5194/acp-18-9681-2018).

- 379 Bellouin, N., Boucher, O., Vesperini, M., & Tanré, D. (2004). Estimating the direct aerosol
380 radiative perturbation: Impact of ocean surface representation and aerosol non-sphericity.
381 *Quarterly Journal of the Royal Meteorological Society*, 130: 2217–2232.
382 doi:10.1256/qj.03.136.
- 383 Bohren, C. F., & Huffman, D. R. (1983). Absorption and scattering of light by small particles,
384 Wiley, New York.
- 385 Boucher, O., et al. (2013). Clouds and Aerosols. In: Climate Change 2013: The Physical Science
386 Basis. Contribution of Working Group I to the Fifth Assessment Report of the
387 Intergovernmental Panel on Climate Change [Stocker, T.F., D. Qin, G.-K. Plattner, M. Tignor,
388 S.K. Allen, J. Boschung, A. Nauels, Y. Xia, V. Bex and P.M. Midgley (eds.)]. Cambridge
389 University Press, Cambridge, United Kingdom and New York, NY, USA.
- 390 Brindley, H.E., & Russell, J.E. (2009). An assessment of Saharan dust loading and the
391 corresponding cloud-free longwave direct radiative effect from geostationary satellite
392 observations. *Journal of Geophysical Research: Atmosphere*, 114, D23201,
393 doi:10.1029/2008JD011635.
- 394 Chen, G., Ziemba, L.D., Chu, D.A., Thornhill, K.L., Schuster, G.L., Winstead, E.L., et al. (2011).
395 Observations of Saharan dust microphysical and optical properties from the Eastern Atlantic
396 during NAMMA airborne field campaign. *Atmospheric Chemistry and Physics*, 11, 723–740,
397 <https://doi.org/10.5194/acp-11-723-2011>.
- 398 Chou C., Formenti, P., Maillé, M., Ausset, P., Helas, G., Harrison, M., & Osborne, S. (2008). Size
399 distribution, shape, and composition of mineral dust aerosols collected during the African
400 Monsoon Multidisciplinary Analysis Special Observation Period 0: Dust and Biomass-Burning
401 Experiment field campaign in Niger, January 2006. *Journal of Geophysical Research:
402 Atmosphere*, 113, D00C10, doi:10.1029/2008JD009897.
- 403 Christopher, S.A., & Jones, T. (2007). Satellite-based assessment of cloud-free net radiative effect
404 of dust aerosols over the Atlantic Ocean. *Geophysical Research Letters*, 34, L02810,
405 doi:10.1029/2006GL027783.
- 406 Colarco, P. R., Nowottnick, E. P., Randles, C. A., Yi, B., Yang, P., Kim, K.-M., Smith, J. A., &
407 Bardeen, C. G. (2014). Impact of radiatively interactive dust aerosols in the NASA GEOS-5
408 climate model: Sensitivity to dust particle shape and refractive index. *Journal of Geophysical
409 Research: Atmosphere*, 119, 753–786, doi:10.1002/2013JD020046.
- 410 d’Almeida, G. A., P. Koepke, & E. P. Shettle (1991). Atmospheric Aerosols: Global Climatology
411 and Radiative Characteristics. A. Deepak Pub, Hampton, 561 p.
- 412 Denjean, C., Cassola, F., Mazzino, A., Triquet, S., Chevaillier, S., Grand, N., et al. (2016a). Size
413 distribution and optical properties of mineral dust aerosols transported in the western
414 Mediterranean. *Atmospheric Chemistry and Physics*, 16, 1081–1104,
415 <https://doi.org/10.5194/acp-16-1081-2016>.
- 416 Denjean, C., Formenti, P., Desboeufs, K., Chevaillier, S., Triquet, S., Maillé, M., et al. (2016b).
417 Size distribution and optical properties of African mineral dust after intercontinental transport.
418 *Journal of Geophysical Research: Atmosphere*, 121, 7117–7138, doi: 10.1002/2016JD024783.
- 419 Di Biagio, C., di Sarra, A., & Meloni, D. (2010) Large atmospheric shortwave radiative forcing
420 by Mediterranean aerosols derived from simultaneous ground-based and spaceborne
421 observations and dependence on the aerosol type and single scattering albedo. *Journal of
422 Geophysical Research: Atmosphere*, 115, D10209, doi:10.1029/2009JD012697.

- 423 Di Biagio, C., Boucher, H., Caquineau, S., Chevaillier, S., Cuesta, J., & Formenti, P. (2014a).
424 Variability of the infrared complex refractive index of African mineral dust: experimental
425 estimation and implications for radiative transfer and satellite remote sensing. *Atmospheric*
426 *Chemistry and Physics*, 14, 11093–11116, <https://doi.org/10.5194/acp-14-11093-2014>.
- 427 Di Biagio, C., Formenti, P., Styler, E., Pangui, E., & Doussin, J.-F. (2014b). Laboratory chamber
428 measurements of the longwave extinction spectra and complex refractive indices of African and
429 Asian mineral dusts. *Geophysical Research Letters*, 41, 6289–6297,
430 doi:10.1002/2014GL060213.
- 431 Di Biagio, C., Formenti, P., Balkanski, Y., Caponi, L., Cazaunau, M., Pangui, E., et al. (2017).
432 Global scale variability of the mineral dust long-wave refractive index: a new dataset of in situ
433 measurements for climate modeling and remote sensing. *Atmospheric Chemistry and Physics*,
434 17, 1901–1929, <https://doi.org/10.5194/acp-17-1901-2017>.
- 435 Di Biagio, C., Formenti, P., Balkanski, Y., Caponi, L., Cazaunau, M., Pangui, E., et al. (2019).
436 Complex refractive indices and single scattering albedo of global dust aerosols in the shortwave
437 spectrum and relationship to iron content and size, *Atmospheric Chemistry and Physics*
438 *Discussion*, <https://doi.org/10.5194/acp-2019-145>.
- 439 di Sarra, A., Pace, G., Meloni, D., De Silvestri, L., Piacentino, S., & Monteleone, F. (2008).
440 Surface shortwave radiative forcing of different aerosol types in the central Mediterranean,
441 *Geophysical Research Letters*, 35, L02714, doi:10.1029/2007GL032395.
- 442 Dubovik, O., Holben, B., Eck, T.F., Smirnov, A., Kaufman, Y.J., King, M.D., Tanré, D., &
443 Slutsker, I. (2002). Variability of absorption and optical properties of key aerosol types
444 observed in worldwide locations. *Journal of the Atmospheric Science*, 59, 590–608,
445 [https://doi.org/10.1175/1520-0469\(2002\)059<0590:VOAAOP>2.0.CO;2](https://doi.org/10.1175/1520-0469(2002)059<0590:VOAAOP>2.0.CO;2).
- 446 Dubovik, O., Sinyuk, A., Lapyonok, T., Holben, B.N., Mishchenko, M., Yang, P., et al. (2006).
447 Application of spheroid models to account for aerosol particle nonsphericity in remote sensing
448 of desert dust, *Journal of Geophysical Research: Atmosphere*, 111, D11208,
449 doi:[10.1029/2005JD006619](https://doi.org/10.1029/2005JD006619).
- 450 Dufresne, J.L., Gautier, C., Ricchiazzi, P. & Fouquart, Y. (2002). Longwave scattering effects of
451 mineral aerosols. *Journal of the Atmospheric Science*, 59, 1959–1966,
452 [https://doi.org/10.1175/1520-0469\(2002\)059<1959:LSEOMA>2.0.CO;2](https://doi.org/10.1175/1520-0469(2002)059<1959:LSEOMA>2.0.CO;2).
- 453 Escribano, J., Boucher, O., Chevaillier, F., & Huneus, N. (2017). Impact of the choice of the
454 satellite aerosol optical depth product in a sub-regional dust emission inversion. *Atmospheric*
455 *Chemistry and Physics*, 17, 7111–7126, <https://doi.org/10.5194/acp-17-7111-2017>.
- 456 Formenti, P., Andreae, M. O., Lange, L., Roberts, G., Cafmeyer, J., Rajta, I., Maenhaut, W.,
457 Holben, B. N., Artaxo, P., & Lelieveld, J. (2001). Saharan dust in Brazil and Suriname during
458 the Large-Scale Biosphere-Atmosphere Experiment in Amazonia (LBA) - Cooperative LBA
459 Regional Experiment (CLAIRE) in March 1998. *Journal of Geophysical Research:*
460 *Atmosphere*, 106(D14), 14919–14934, doi: 10.1029/2000JD900827.
- 461 Formenti, P., Rajot, J. L., Desboeufs, K., Saïd, F., Grand, N., Chevaillier, S., & Schmechtig, C
462 (2011). Airborne observations of mineral dust over western Africa in the summer Monsoon
463 season: spatial and vertical variability of physico-chemical and optical properties. *Atmospheric*
464 *Chemistry and Physics*, 11, 6387–6410, <https://doi.org/10.5194/acp-11-6387-2011>.
- 465 Fouquart, Y. and Bonnel, B. (1980) Computations of Solar Heating of the Earth's Atmosphere—
466 A New Parameterization. *Beitrage zur Physik der Atmosphäre*, 53, 35–62.

467 Fratini, G., Ciccioli, P., Febo, A., Forgiione, A. & R. Valentini (2007). Size-segregated fluxes of
468 mineral dust from a desert area of northern China by eddy covariance. *Atmospheric Chemistry*
469 *and Physics*, 7, 2839–2854, <https://doi.org/10.5194/acp-7-2839-2007>.

470 Fu, Q., and K. N. Liou (1993), Parameterization of the radiative properties of cirrus clouds, J.
471 Atmos. Sci., 50, 2008 – 2025, doi:10.1175/1520-0469(1993)050<2008:POTRPO>2.0.CO;2.

472 Gillette, D.A., Blifford, I.H. & Fenster, C.R. (1972). Measurements of aerosol size distributions
473 and vertical fluxes of aerosols on land subject to wind erosion. *Journal of Applied Meteorology*,
474 11, 977–987, [https://doi.org/10.1175/1520-0450\(1972\)011<0977:MOASDA>2.0.CO;2](https://doi.org/10.1175/1520-0450(1972)011<0977:MOASDA>2.0.CO;2).

475 Gillette, D.A., Blifford, I.H. & Fryrear, D.W. (1974a). Influence of wind velocity on size
476 distributions of aerosols generated by wind erosion of soils. *Journal of Geophysical Research:*
477 *Atmosphere* , 79, 4068–4075, doi:10.1029/JC079i027p04068.

478 Gillette, D.A. (1974b), On the production of soil wind erosion having the potential for long range
479 transport. *Journal of Geophysical Research: Atmosphere*, 8, 734–744.

480 Granados-Muñoz, M. J., Sicard, M., Román, R., Benavent-Oltra, J. A., Barragán, R., Brogniez,
481 G., et al. (2019). Impact of mineral dust on shortwave and longwave radiation: evaluation of
482 different vertically resolved parameterizations in 1-D radiative transfer computations.
483 *Atmospheric Chemistry and Physics*, 19, 523–542, <https://doi.org/10.5194/acp-19-523-2019>.

484 Hansell, R.A., Tsay, S.C., Ji, Q., Hsu, N.C., Jeong, M.J., Wang, S.H., Reid, J.S., Liou, K.N., &
485 Ou, S.C. (2010). An Assessment of the Surface Longwave Direct Radiative Effect of Airborne
486 Saharan Dust during the NAMMA Field Campaign. *Journal of the Atmospheric Science*, 67,
487 1048–1065, <https://doi.org/10.1175/2009JAS3257.1>.

488 Hansell, R. A., et al. (2012), An assessment of the surface longwave direct radiative effect of
489 airborne dust in Zhangye, China, during the Asian Monsoon Years field experiment (2008),
490 *Journal of Geophysical Research: Atmosphere* , 117, D00K39, doi:10.1029/2011JD017370.

491 Hess, M., P. et al. (1998), Optical properties of aerosols and clouds: The software package OPAC.
492 *Bulletin of the American Meteorological Society*, 79(5), 831–844,
493 [https://doi.org/10.1175/1520-0477\(1998\)079<0831:OPOAAC>2.0.CO;2](https://doi.org/10.1175/1520-0477(1998)079<0831:OPOAAC>2.0.CO;2).

494 Hourdin, F., Mauritsen, T., Gettelman, A., Golaz, J.-C., Balaji, V., Duan, Q., et al. (2017). The art
495 and science of climate model tuning. *Bulletin of the American Meteorological*
496 *Society*, 98(3), 589–602, <https://doi.org/10.1175/bams-d-15-00135.1>.

497 Huneeus, N., Schulz, M., Balkanski, Y., Griesfeller, J., Prospero, J., Kinne, S., et al. (2011). Global
498 dust model intercomparison in AeroCom phase I, *Atmospheric Chemistry and Physics*, 11(15),
499 7781–7816, doi:10.5194/acp-11-7781-2011.

500 Kandler, K. , Lieke, K. , Benker, N. , Emmel, C. , Küpper, M. , Müller-Ebert, D., et al. (2011),
501 Electron microscopy of particles collected at Praia, Cape Verde, during the Saharan Mineral
502 Dust Experiment: particle chemistry, shape, mixing state and complex refractive index. *Tellus*
503 *B*, 63: 475–496. doi:10.1111/j.1600-0889.2011.00550.x.

504 Kaufman, Y. J., Koren, I., Remer, L. A., Tanre, D., Ginoux, P., & Fan, S. (2005). Dust transport
505 and deposition observed from the Terra-Moderate Resolution Imaging Spectroradiometer
506 (MODIS) spacecraft over the Atlantic Ocean. *Journal of Geophysical Research: Atmosphere*,
507 110, D10S12, doi:10.1029/2003JD004436.

508 Koffi, B., et al. (2012), Application of the CALIOP layer product to evaluate the vertical
509 distribution of aerosols estimated by global models: AeroCom phase I results, *J. Geophys. Res.*,
510 117, D10201, doi:10.1029/2011JD016858.

511 Kok, J. F. (2011). A scaling theory for the size distribution of emitted dust aerosols suggests
512 climate models underestimate the size of the global dust cycle. *Proceedings of the National*
513 *Academy of Sciences*, 108(3), 1016, <https://doi.org/10.1073/pnas.1014798108>.

514 Kok, J. F., Ridley, D. A., Zhou, Q., Miller, R. L., Zhao, C., Heald, C. L., Ward, D. S., Albani, S.,
515 & Haustein, K. (2017). Smaller desert dust cooling effect estimated from analysis of dust size
516 and abundance. *Nature Geoscience*, 10, 274–278, <https://doi.org/10.1038/ngeo2912>.

517 Li, F., Vogelmann, A.M., & Ramanathan, V. (2004). Saharan Dust Aerosol Radiative Forcing
518 Measured from Space. *Journal of Climate*, 17, 2558–2571, [https://doi.org/10.1175/1520-0442\(2004\)017<2558:SDARFM>2.0.CO;2](https://doi.org/10.1175/1520-0442(2004)017<2558:SDARFM>2.0.CO;2).

520 Liao, H., & Seinfeld, J. H. (1998). Radiative forcing by mineral dust aerosols: sensitivity to key
521 variables. *Journal of Geophysical Research: Atmosphere*, 103, 31637–31646,
522 doi:10.1029/1998JD200036.

523 Liuzzi, G., Masiello, G., Serio, C., Meloni, D., Di Biagio, C., & Formenti, P. (2017), Consistency
524 of dimensional distributions and refractive indices of desert dust measured over Lampedusa
525 with IASI radiances. *Atmospheric Measurements Techniques*, 10, 599–615,
526 <https://doi.org/10.5194/amt-10-599-2017>.

527 Mahowald, N., Albani, S., Kok, J. F., Engelstaedter, S., Scanza, R., Ward, D. S., & Flanner, M. G.
528 (2014). The size distribution of desert dust aerosols and its impact on the Earth system. *Aeolian*
529 *Research*, 15, 53–71, doi: 10.1016/j.aeolia.2013.09.002.

530 Maring, H., Savoie, D. L., Izaguirre, M. A., Custals, L., & Reid, J. S. (2003). Mineral dust aerosol
531 size distribution change during atmospheric transport, *Journal of Geophysical Research:*
532 *Atmosphere*, 108, 8592, doi:10.1029/2002jd002536.

533 Meloni, D., di Sarra, A., Brogniez, G., Denjean, C., De Silvestri, L., Di Iorio, T., et al. (2018).
534 Determining the infrared radiative effects of Saharan dust: a radiative transfer modelling study
535 based on vertically resolved measurements at Lampedusa. *Atmospheric Chemistry and Physics*,
536 18, 4377–4401, <https://doi.org/10.5194/acp-18-4377-2018>.

537 Miller, R. L., Tegen, I., & Perlwitz, J. (2004). Surface radiative forcing by soil dust aerosols and
538 the hydrologic cycle. *Journal of Geophysical Research: Atmosphere* , 109, D04203,
539 doi:10.1029/2003JD004085.

540 Miller, R.L., Cakmur, R.V., Perlwitz, J.P., Geogdzhayev, I.V., Ginoux, P., Kohfeld, K.E., et al.
541 (2006). Mineral dust aerosols in the NASA Goddard Institute for Space Sciences ModelE
542 atmospheric general circulation model. *Journal of Geophysical Research: Atmosphere*, 111,
543 D06208, doi:10.1029/2005JD005796.

544 Osipov, S., Stenchikov, G., Brindley, H., and Banks, J. (2015). Diurnal cycle of the dust
545 instantaneous direct radiative forcing over the Arabian Peninsula. *Atmospheric Chemistry and*
546 *Physics*, 15, 9537–9553, <https://doi.org/10.5194/acp-15-9537-2015>.

547 Patadia, F., Yang, E.-S., & Christopher, S.A. (2009). Does dust change the clear sky top of
548 atmosphere shortwave flux over high surface reflectance regions? *Geophysical Research*
549 *Letters*, 36, L15825, doi:10.1029/2009GL039092.

550 Patterson, E.M., Filette, D. A., & Stockton, B. H. (1977). Complex index of refraction between
551 300 and 700 nm for Saharan aerosols. *Journal of Geophysical Research: Atmosphere*, 82,
552 3153–3160, 1977, doi:10.1029/JC082i021p03153.

553 Potenza, M.A.C., Albani, S., Delmonte, B., Villa, S., Sanvito, T., Paroli, B., Pullia, A., Baccolo,
554 G., Mahowald, N., & Maggi, V. (2016). Shape and size constraints on dust optical properties
555 from the Dome C ice core, Antarctica. *Scientific Reports*, 6, 28162; doi: 10.1038/srep28162.

556 Rajeev, K., and V. Ramanathan, 2001: Direct observations of clearsky aerosol radiative forcing
557 from space during the Indian Ocean experiment. *J. Geophys. Res.*, 106, 17 221–17 235,
558 doi:10.1029/2000JD900723.

559 Ridley, D. A., Heald, C. L., Kok, J. F., & Zhao, C. (2016). An observationally–constrained
560 estimate of global dust aerosol optical depth. *Atmospheric Chemistry and Physics*, 16,
561 15097_15117, <https://doi.org/10.5194/acp-16-15097-2016>.

562 Rosenberg, P. D., Parker, D. J., Ryder, C. L., Marsham, J. H., Garcia-Carreras, L., Dorsey, J. R.,
563 et al. (2014). Quantifying particle size and turbulent scale dependence of dust flux in the Sahara
564 using aircraft measurements. *Journal of Geophysical Research: Atmosphere*, 119, 7577–7598,
565 doi:10.1002/2013JD021255.

566 Ryder, C. L., Highwood, E. J., Rosenberg, P. D., Trembath, J., Brooke, & J. K., Bart (2013a).
567 Optical properties of Saharan dust aerosol and contribution from the coarse mode as measured
568 during the Fennec 2011 aircraft campaign. *Atmospheric Chemistry and Physics*, 13, 303–325,
569 <https://doi.org/10.5194/acp-13-303-2013>.

570 Ryder, C. L., Highwood, E. J., Lai, T. M., Sodemann, H., & Marsham, J. H. (2013b). Impact of
571 atmospheric transport on the evolution of microphysical and optical properties of Saharan dust.
572 *Geophysical Research Letters*, 40, 2433– 2438, doi:10.1002/grl.50482.

573 Ryder, C. L., Marengo, F., Brooke, J. K., Estelles, V., Cotton, R., Formenti, P., et al. (2018).
574 Coarse–mode mineral dust size distributions, composition and optical properties from AER–D
575 aircraft measurements over the tropical eastern Atlantic. *Atmospheric Chemistry and Physics*,
576 18, 17225–17257, <https://doi.org/10.5194/acp-18-17225-2018>.

577 Ryder, C. L., Highwood, E. J., Walser, A., Seibert, P., Philipp, A., & Weinzierl, B. (2019). Coarse
578 and Giant Particles are Ubiquitous in Saharan Dust Export Regions and are Radiatively
579 Significant over the Sahara. *Atmospheric Chemistry and Physics Discussion*,
580 <https://doi.org/10.5194/acp-2019-421>.

581 Satheesh, S. K., & V. Ramanathan (2000). Large differences in tropical aerosol forcing at the top
582 of the atmosphere and Earth’s surface, *Nature*, 405, 60–63, doi:10.1038/35011039.

583 Schulz, M. (2007). Constraining Model Estimates of the Aerosol Radiative Forcing, Thèse
584 d’Habilitation à Diriger des Recherches, Université Pierre et Marie Curie, Paris VI.

585 Séférian, R., Baek, S., Boucher, O., Dufresne, J.–L., Decharme, B., Saint–Martin, D., & Roehrig,
586 R. (2018). An interactive ocean surface albedo scheme (OSAv1.0): formulation and evaluation
587 in ARPEGE–Climat (V6.1) and LMDZ (V5A), *Geoscientific Model Development*, 11, 321–
588 338, <https://doi.org/10.5194/gmd-11-321-2018>.

589 Shao, Y., Ishizuka, M., Mikami, M. & Leys, J.F. (2011). Parameterization of size–resolved dust
590 emission and validation with measurements. *Journal of Geophysical Research–Atmospheres*,
591 116, D08203, doi:10.1029/2010JD014527.

592 Shettle, P. E. & Fenn, R. W. (1979). Models for the aerosols of the lower atmosphere and the
593 effects of humidity variations on their optical properties. AFCRL Tech. Report, 79 0214,
594 Research Papers No. 676, Air Force Cambridge Research Laboratory, Hanscom Airforce Base,
595 MA., 100 pp.

596 Sicard, M., Bertolín, S., Mallet, M., Dubuisson, P., & Comerón, A. (2014). Estimation of mineral
597 dust long-wave radiative forcing: sensitivity study to particle properties and application to real
598 cases in the region of Barcelona. *Atmospheric Chemistry and Physics*, 14, 9213–9231,
599 <https://doi.org/10.5194/acp-14-9213-2014>.

600 Sokolik, I., & Toon, O. (1999). Incorporation of mineralogical composition into models of the
601 radiative properties of mineral aerosol from UV to IR wavelengths. *Journal of Geophysical*
602 *Research: Atmosphere*, 104(D8), 9423–9444.

603 Song, Q., Zhang, Z., Yu, H., Kato, S., Yang, P., Colarco, P., Remer, L. A., & Ryder, C. L. (2018).
604 Net radiative effects of dust in the tropical North Atlantic based on integrated satellite
605 observations and in situ measurements. *Atmospheric Chemistry and Physics*, 18, 11303–11322,
606 <https://doi.org/10.5194/acp-18-11303-2018>.

607 Sow, M., Alfaro, S.C., Rajot, J.L. & Marticorena, B. (2009). Size resolved dust emission fluxes
608 measured in Niger during 3 dust storms of the AMMA experiment. *Atmospheric Chemistry and*
609 *Physics*, 9, 3881–3891, <https://doi.org/10.5194/acp-9-3881-2009>.

610 Stier, P., Schutgens, N. A. J., Bellouin, N., Bian, H., Boucher, O., Chin, M., et al. (2013). Host
611 model uncertainties in aerosol radiative forcing estimates: results from the AeroCom Prescribed
612 intercomparison study. *Atmospheric Chemistry and Physics*, 13, 3245–3270,
613 <https://doi.org/10.5194/acp-13-3245-2013>.

614 van der Does, M., Knippertz, P. Zschenderlein, P. Giles Harrison R. & Stuut J.–B. W. (2018). The
615 mysterious long-range transport of giant mineral dust particles, *Science Advances*, 4, 12, DOI:
616 10.1126/sciadv.aau2768.

617 Volz, F. E. (1972), Longwave refractive index of atmospheric aerosol substances, *Appl. Opt.*, 11,
618 755–759, <https://doi.org/10.1364/AO.11.000755>.

619 Volz, F. E. (1973). Longwave optical constants of ammonium sulfate, Sahara dust; volcanic
620 pumice and flyash. *Applied Optics*, 12, 564–568, <https://doi.org/10.1364/AO.12.000564>.

621 Wang, J., Doussin, J. F., Perrier, S., Perraudin, E., Katrib, Y., Pangui, E., & Picquet–Varrault, B.
622 (2011). Design of a new multi-phase experimental simulation chamber for atmospheric
623 photochemistry, aerosol and cloud chemistry research. *Atmospheric Measurements Techniques*, 4,
624 2465–2494, doi:10.5194/amt-4-2465-2011.

625 Weinzierl, B., Petzold, A., Esselborn, M., Wirth, M., Rasp, K., Kandler, K., et al. (2009).
626 Airborne measurements of dust layer properties, particle size distribution and mixing state of
627 Saharan dust during SAMUM 2006. *Tellus B*, 61B, 96–117, doi:10.1111/j.1600-
628 0889.2008.00392.x.

629 Weinzierl, B., Sauer, D., Esselborn, M., Petzold, A., Veira, A., Rose, M., et al. (2011).
630 Microphysical and optical properties of dust and tropical biomass burning aerosol layers in the
631 Cape Verde region – An overview of the airborne in-situ and lidar measurements during
632 SAMUM-2. *Tellus B*, 63B(4), 589–618, <http://dx.doi.org/10.1111/j.16000889.2011.00566.x>

633 Weinzierl, B., Ansmann, A., Prospero, J. M., Althausen, D., Benker, N., Chouza, F., et al. (2017).
634 The Saharan Aerosol Long-range Transport and Aerosol–cloud–interaction experiment:
635 Overview and Selected Highlights, *Bulletin of the American Meteorological Society*, 98, 1427–
636 1451, doi: 10.1175/BAMS-D-15-00142.

637 Yang, E.–S., Gupta, P., & Christopher, S.A. (2009). Net radiative effect of dust aerosols from
638 satellite measurements over Sahara. *Geophysical Research Letters*, 36, L18812,
639 doi:10.1029/2009GL039801.

- 640 Zhang, J., & Christopher, S.A. (2003). Longwave radiative forcing of Saharan dust aerosols
641 estimated from MODIS, MISR, and CERES observations on Terra. *Geophysical Research*
642 *Letters*, 30(23), 2188, doi:10.1029/2003GL018479.
- 643 Zhang, L., Li, Q. B., Gu, Y., Liou, K. N., & Meland, B. (2013). Dust vertical profile impact on
644 global radiative forcing estimation using a coupled chemical–transport–radiative–transfer
645 model. *Atmospheric Chemistry and Physics*, 13, 7097–7114, [https://doi.org/10.5194/acp-13-](https://doi.org/10.5194/acp-13-7097-2013)
646 [7097–2013](https://doi.org/10.5194/acp-13-7097-2013).